Nanoscale

PAPER

Cite this: *Nanoscale*, 2016, **8**, 1658

Plasmonic gold nanoparticles for ZnO-nanotube photoanodes in dye-sensitized solar cell application†

Marwa Abd-Ellah, Nafiseh Moghimi, Lei Zhang, Joseph. P. Thomas, Donald McGillivray, Saurabh Srivastava and Kam Tong Leung*

Received 13th November 2015,
Accepted 9th December 2015

DOI: 10.1039/c5nr08029k

www.rsc.org/nanoscale

Surface modification of nanostructured metal oxides with metal nanoparticles has been extensively used to enhance their nanoscale properties. The unique properties of metal nanoparticles associated with their controllable dimensions allow these metal nanoparticles to be precisely engineered for many applications, particularly for renewable energy. Here, a simple electrodeposition method to synthesize gold nanoparticles (GNPs) on electrochemically grown ZnO nanotubes (NTs) is reported. The size distribution and areal density of the GNPs can be easily controlled by manipulating the concentration of $AuCl_3$ electrolyte solution, and the deposition time, respectively. An excellent enhancement in the optical properties of ZnO NTs surface-decorated with GNPs (GNP/ZnO-NT), especially in the visible region, is attributed to their surface plasmon resonance. The plasmonic effects of GNPs, together with the large specific surface area of ZnO NTs, can be used to significantly enhance the dye-sensitized solar cell (DSSC) properties. Furthermore, the Schottky barrier at the Au/ZnO interface could prevent electron back transfer from the conduction band of ZnO to the redox electrolyte and thus could substantially increase electron injection in the ZnO conduction band, which would further improve the overall performance of the constructed DSSCs. The GNP/ZnO-NT photoanode has been found to increase the efficiency of the DSSC significantly to 6.0% from 4.7% of the pristine ZnO-NT photoanode, together with corresponding enhancements in short-circuit current density from 10.4 to 13.1 mA cm^{-2} and in fill factor from 0.60 to 0.75, while the open-circuit voltage remain effectively unchanged (from 0.60 to 0.61 V). Surface decoration with GNPs therefore provides an effective approach to creating not only a high specific surface area for superior loading of dye molecules, but also higher absorbance capability due to their plasmonic effect, all of which lead to excellent performance enhancement for DSSC application.

1 Introduction

Nanoplasmonics is a rapidly growing research field that exploits enhancement of concentrated optical energy on the nanoscale in nanostructured metal systems arising from their surface plasmon modes.[1–4] Recently, gold nanoparticles (GNPs) have been introduced to different materials to improve their sensing, photocatalytic, and optical properties.[5–7] One of the major applications that take advantage of their improved light absorption capability specifically in the visible region is photovoltaics.[8–11] Surface modification with plasmonic nanoparticles was first introduced to photovoltaics for enhancing inorganic thin-film solar cells, particularly by compensating the loss of absorption with reduction in the absorber thickness.[12–16] Furthermore, GNPs have been used in both polymer-based and dye-based organic photovoltaics to provide a significant improvement in their performance.[17–21] In a typical dye-sensitized solar cell (DSSC), the dye molecules adsorbed on the photoanode surface are the main photon absorbers that can be excited, which results in the injection of their excited electrons into the conduction band of the semiconductor material. The injected electrons are easily transported from the photoanode *via* the back contact (usually made up of a transparent conductive oxide material) to the Pt counter electrode. The process can be repeated by simple regeneration of the dye molecules using a redox couple ($3I^-/I_3^-$) liquid electrolyte, followed by reduction of the electrolyte with the catalytically active Pt electrode.[22] Au–SiO_2 core–shell NPs have been used as a plasmonic light harvesting

WATLab and Department of Chemistry, University of Waterloo, Waterloo, Ontario, N2L3G1 Canada. E-mail: tong@uwaterloo.ca

†Electronic supplementary information (ESI) available: UV/Vis absorption spectra of GNP/ZnO-NT photoanodes with GNPs obtained with deposition for 30, 60, 300, and 600 s, showing the similar absorbance in the visible region for deposition time above 300 s (Fig. S1); current density *vs.* voltage profile of GNP/ZnO-NT based DSSC with agglomerated GNPs obtained by using a 10 mM $AuCl_3$ electrolyte. (Fig. S2); and UV/Vis absorption spectra of pristine ZnO-NT and GNP/ZnO-NT samples (Fig. S3). See DOI: 10.1039/c5nr08029k

antenna on a TiO_2 NP photoanode for liquid and solid-state based DSSCs. An improved efficiency approaching 1.95% (from 1.05%) was obtained for the N719 dye with the ($3I^-/I_3^-$) liquid electrolyte in a liquid-based DSSC.[23] An efficiency enhancement approaching 2.2% (from 1.2%) was also obtained when the Z907 dye was employed for solid-state based DSSCs.[23] Recently, ZnO has been used as an alternative n-type semiconducting photoanode material for DSSCs, because of its similar bandgap, higher electron dynamics, and a versatile nanostructural morphology relative to TiO_2.[24–27] Further modifications have been performed by mixing with other nanostructured metal oxides (such as TiO_2 and SnO_2) or with metallic NPs (including Au and Ag) for improving their charge carrier and absorption properties for DSSC application.[28–31] Coating of vertically aligned ZnO nanorods with GNPs using an "all-hydrothermal" method was reported to increase the photon conversion efficiency from 0.7% to 1.2%, along with an increase in its open-circuit voltage from 0.50 to 0.63 V.[32] Here, we develop a successive electrodeposition procedure to decorate with GNPs the high-surface-area ZnO NTs, also obtained by direct electrodeposition, and demonstrate its advantage as an effective DSSC photoanode. As electrodeposition is capable of preparing high-quality nanomaterials with better crystallinity and minimum lattice mismatch, the resulting enhanced interface quality could also improve the contact of GNPs on the ZnO NT surface. This leads to lower resistance for better electron conduction that is important for advanced electronic device applications. The GNP particle size can be easily optimized with different concentrations of $AuCl_3$ in $NaClO_4$ mixed with the 0.1 M KCl electrolyte, while its areal density can be controlled by the deposition time at a selected $AuCl_3$ concentration (1 mM). Our results illustrate the many advantages of our all-electrochemically-grown GNP/ZnO-NT photoanode, as provided by their better capacity for dye loading and higher charge transport inherent in the one-dimensional, high-specific-surface-area ZnO NTs, and by the pronounced enhancement in their absorption due to the surface plasmonic effect of the GNPs. With the Schottky barrier build up at the Au/ZnO interface, a higher electron density is also obtained at the ZnO conduction band due to the reduction of electron-transfer resistance and minimization of recombination loss by blocking the back electron transfer from ZnO to the electrolyte or/and the dye molecules. An increase by almost 28% in the overall efficiency, from 4.7% for pristine ZnO-NT DSSC to 6.0% for GNP/ZnO-NT DSSC, can be achieved.

2 Experimental

For all sample preparations, a three-electrode electrochemical cell, with an ITO-glass working electrode, an Ag/AgCl reference electrode, and a Pt-wire counter electrode, in an electrochemical workstation (CH Instruments 1140) was employed. The preparation of ZnO NTs on ITO-glass substrates by electrochemical deposition has been discussed in detail elsewhere.[27] Briefly, by delicately controlling the electrolyte conductivity with different mono and divalent supporting electrolytes in the same 0.5 mM $ZnCl_2$ primary electrolyte, we showed that it was possible to manipulate the growth mechanism and to obtain directly electrodeposited ZnO nanotubes. Gold nanoparticles were then electrodeposited on the ZnO NTs in an aqueous solution of 1, 5, or 10 mM $AuCl_3$ in 0.1 M $NaClO_4$ and 0.1 M KCl by potentiostatic amperometry (at −1.0 V *vs.* Ag/AgCl) at room temperature for 60 s. After deposition, the as-prepared samples were rinsed thoroughly in filtered deionized water and stored under a nitrogen atmosphere to dry for at least 24 hours prior to characterization.

The surface morphologies were examined by using helium ion microscopy (HIM) with a Zeiss Orion Plus microscope and field-emission scanning electron microscopy (SEM) with a Zeiss Merlin microscope. Bright-field high-resolution transmission electron microscopy (TEM) studies were performed by using a Zeiss Libra 200 MC microscope on GNP/ZnO-NT nanostructures scraped off from the substrate and transferred onto a lacey-carbon TEM grid. The corresponding crystal structures were characterized by glancing-incidence X-ray diffraction (XRD) using a PANalytical X'Pert Pro MRD diffractometer with Cu Kα radiation (1.54 Å) at an incidence angle of 0.6°. The surface compositions of the GNP/ZnO-nanodeposits were analyzed by X-ray photoelectron spectroscopy (XPS) using a Thermo-VG Scientific ESCALab 250 Microprobe with a monochromatic Al Kα source (1486.6 eV). Cyclic voltammetry and electrochemical impedance spectroscopy were performed in 10 mM $K_3Fe(CN)_6$ in a PBS solution (pH = 7.4) using the same electrochemical workstation. The optical properties were investigated by using a Perkin Elmer Lambda 1050 UV/Vis spectrometer.

Typical DSSCs were fabricated using a standard procedure.[33] After the preparation of GNP/ZnO-NT on an ITO-glass substrate, the photoanode was annealed at 130 °C for 30 min to improve their dye loading properties and their contact with the substrate. The working electrode was constructed by dipping the resulting GNP/ZnO-NT photoanode in a 0.5 mM solution of commercial dye N719 (purchased from Sigma Aldrich) for 2 h. The counter electrode was obtained by sputter-coating a Pt thin film (200 nm thick) onto another ITO-glass substrate. A redox ($3I^-/I_3^-$) couple electrolyte was then sandwiched between the working and counter electrodes to create the DSSC. The current density *vs.* voltage (*J–V*) characteristics were analyzed using a solar cell I–V measurement system (PV Measurements IV5) equipped with a class ABA solar simulator and an Air Mass (AM) 1.5 global spectral filter. Prior to the *J–V* measurement, the system was calibrated using a Si reference cell (PVM782 with a BK7 window).

3 Results and discussion

3.1. Characterization of GNP/ZnO-NT photoanodes

Fig. 1 shows the SEM images of ZnO NTs electrochemically grown on an ITO-glass substrate with and without subsequent

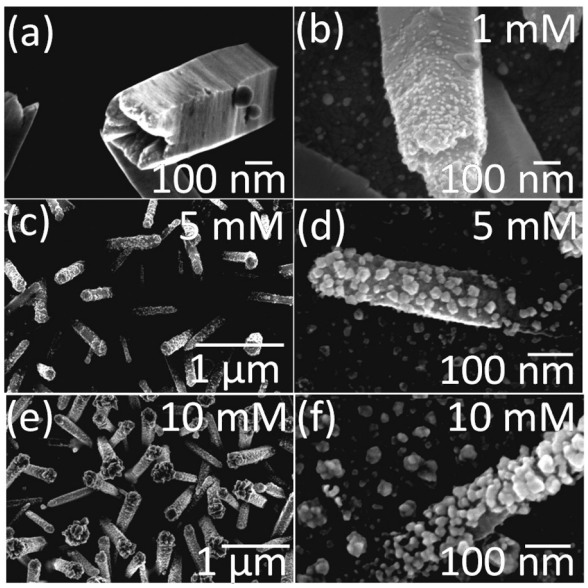

Fig. 1 SEM images of (a) pristine ZnO-NTs, and GNP/ZnO-NTs obtained by GNP electrodeposition in (b) 1 mM, (c, d) 5 mM, and (e, f) 10 mM $AuCl_3$ electrolytes, all mixed with 0.1 M $NaClO_4$ and 0.1 M KCl supporting electrolytes, at room temperature.

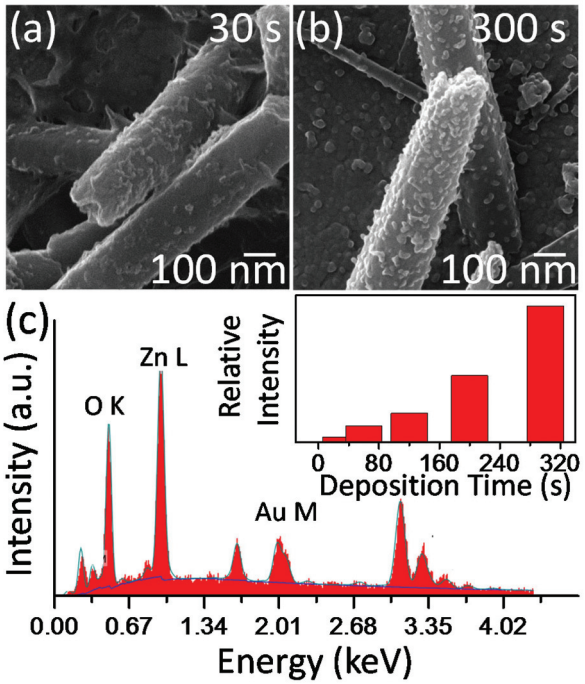

Fig. 2 HIM images of ZnO nanotubes electrodeposited with Au nanoparticles in the 1 mM $AuCl_3$ electrolyte for (a) 30 s and (b) 300 s. (c) Energy-dispersive X-ray spectrum for the ZnO nanotubes decorated with gold nanoparticles obtained by 300 s deposition, with the inset depicting the relative intensity change of the Au M emission feature with respect to the Zn L feature for gold nanoparticle deposition of 30, 60, 120, 200, and 300 s.

electrodeposition of GNPs for 60 s. The resulting ZnO NTs are typically 1–1.5 μm long and 200–500 nm in diameter (Fig. 1a). Different gold electrolyte concentrations have been used for electrodepositing GNPs to obtain different nanoparticle sizes. At the lowest concentration of 1 mM employed in the present study (Fig. 1b), a homogeneous coverage of GNPs on both the inside and outside surfaces near the tip of the ZnO NT is observed. These GNPs also exhibit a fairly uniform spatial distribution on their surface along the length of the nanotube, with an average particle size of 12 nm. Increasing the electrolyte concentration to 5 mM (Fig. 1c and d) produces a higher aerial density and larger GNPs with an average size of 20–50 nm along the entire ZnO NT length. At the highest concentration of 10 mM (Fig. 1e and f), we observe even larger GNPs with an average size over 50 nm. Interestingly, the larger GNPs (>30 nm) obtained with the latter two concentrations also tend to agglomerate on the surface along the length of the ZnO NT, leading to high or even complete coverage of the ZnO NT surfaces, in contrast to that found for the lowest concentration (1 mM). As GNPs could also be electrodeposited on a pristine ITO-glass substrate (*i.e.* without any ZnO NTs), a seed layer of ZnO is pre-electrodeposited prior to the growth of the ZnO nanostructures to ensure that pristine ITO-glass or GNPs on ITO-glass is not involved in the photovoltaic process.

Taking advantage of the higher surface contrast and the superior depth of focus of helium ion microscopy, we study the areal density of GNPs grown on the ZnO NT surfaces, which can be easily increased by increasing the deposition time. As illustrated by the HIM images for GNPs obtained with the 1 mM $AuCl_3$ electrolyte solution, the areal density of GNPs on ZnO NT is significantly higher for 300 s (Fig. 2b) than that for 30 s (Fig. 2a) and that the spatial distribution of GNPs remains uniform on the NT surface. Energy dispersive X-ray elemental analysis has been performed on the GNP/ZnO-NT samples obtained with GNP deposition times of 30, 60, 120, 200, and 300 s. In Fig. 2c the inset shows that a higher relative intensity of the Au peak for the GNP (with respect to the relatively constant Zn and O peak intensities) is obtained for the 300 s deposition, thus confirming the increase of the GNP areal density with the increasing deposition time. However, the higher deposition time (>300 s) is also found to slightly decrease in their light absorbance in the visible region, as shown in their UV/Vis absorption spectra in Fig. S1, ESI,† which is likely due to particle aggregation. To maximize the total surface area of GNPs in order to facilitate maximal loading of the dye in the DSSC fabrication, we select the GNP/ZnO-NT sample deposited with a near-monolayer coverage of the smallest GNPs but with the largest areal density, *i.e.* that obtained by the 300 s deposition (Fig. 2b).

The low-magnification TEM image for the GNP/ZnO-NT photoanode shown in Fig. 3a confirms the existence of the GNPs as-electrodeposited on the ZnO-NT surface with a particle size distribution of 4–22 nm and an average size of 12 nm (Fig. 3a, inset). The corresponding high-resolution TEM images for ZnO NT (Fig. 3b) and GNP (Fig. 3c) reveal sharp fringes with respective spacings of 0.247 nm and 0.235 nm, which are in good accord with the respective interplanar separ-

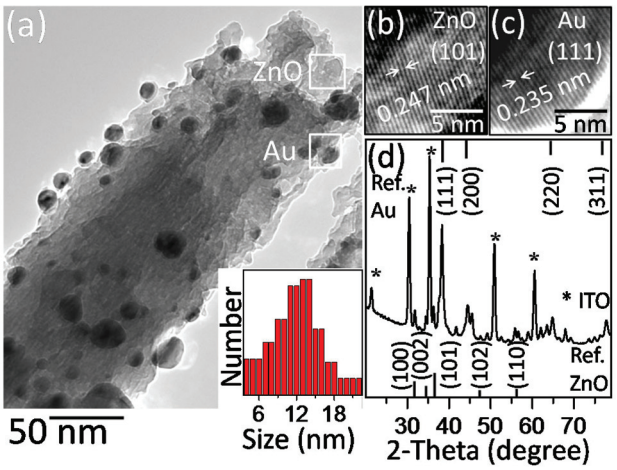

Fig. 3 (a) Low-magnification TEM image of GNP/ZnO-NT, and high-resolution TEM images of (b) selected ZnO-NT and (c) GNP regions, revealing the respective fringe spacings for ZnO(101) and Au(111). (d) Glancing-incidence X-ray diffraction pattern of the GNP/ZnO-NT on ITO-glass substrate, along with the reference patterns for wurtzite ZnO (JCPDS 010790206) and fcc Au (JCPDS 030652870). The diffraction features for ITO are marked by asterisks.

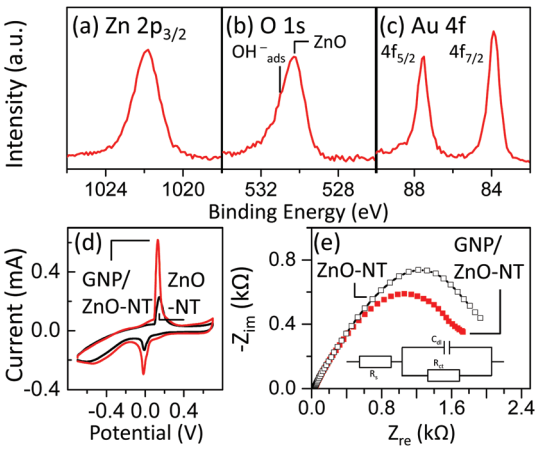

Fig. 4 XPS spectra of (a) Zn $2p_{3/2}$, (b) O 1s, and (c) Au 4f regions for the GNP/ZnO-NT photoanode. (d) Cyclic voltammograms, and (e) Nyquist plots for the GNP/ZnO-NT and pristine ZnO-NT photoanodes, with an inset of their equivalent circuit model.

ations for the ZnO(101) and Au(111) planes. This is also in good agreement with the glancing-incidence XRD pattern of the GNP/ZnO-NT photoanode shown in Fig. 3d. Despite the strong XRD peaks from the ITO substrate, we observe well-defined Au XRD features for (111) at 38.1°, (200) at 44.3°, (220) at 64.5°, and (311) at 77.5°, which are consistent with the reference pattern for the face centered cubic structure of Au (JCPDS 030652870). The weaker peaks at 31.7°, 34.4°, 36.2°, 47.5° and 56.6° correspond, respectively, to the (100), (002), (101), (102) and (110) planes of ZnO, in good accord with the reference pattern for the hexagonal wurtzite structure of ZnO (JCPDS 010790206). The higher intensity ratio for ZnO(101) to ZnO(100) found for the ZnO NTs relative to that for ZnO powder (as shown in the reference pattern) indicates a preferred ZnO growth direction along the [101] direction. Similarly, the higher intensity ratio for Au(111) to Au(200) observed for the GNPs than that for the Au reference reflects preferential growth along the [111] direction for these GNPs, which is likely due to the good lattice match between the Au(111) and ZnO(101) planes.

Fig. 4 shows the XPS chemical-state composition analysis for the GNP/ZnO-NT photoanode. The Zn $2p_{3/2}$ peak near 1021.8 eV corresponds to the Zn^{2+} oxidation state of ZnO (Fig. 4a), while the O 1s peak at 530.2 eV and the weak shoulder at 531.1 eV can be attributed to ZnO and $Zn(OH)_2$, respectively (Fig. 4b). The metallic form of the GNPs is confirmed by the presence of the Au $4f_{7/2}$ ($4f_{5/2}$) feature at 83.8 eV (87.5 eV) (Fig. 4c).[34,35]

Further electrochemical characterization for GNP/ZnO-NT photoanodes has also been performed using 10 mM $K_3[Fe(CN)_6]$ in a 10 mM PBS (pH = 7.4) at room temperature, and the results are compared with those for pristine ZnO-NT photoanodes (*i.e.* without any GNP deposition). The cyclic voltammograms shown in Fig. 4d indicate that both oxidation and reduction currents for GNP/ZnO-NT are considerably larger than that for pristine ZnO-NT. In the electrochemical cell, electrons enter the electrolyte solution and the metal ions start to diffuse into the electrolyte upon dissolution. The rate of charge migration depends on the charge-transfer resistance inside the electrolyte solution. When ZnO NTs are decorated with GNPs, significant enhancement in both oxidation and reduction currents can be observed. The higher current at a fixed potential found for the GNP/ZnO-NT photoanode is due to a lower charge-transfer resistance, when compared to pristine ZnO-NT. Further confirmation is obtained from electrochemical impedance spectroscopy for both photoanodes. Fig. 4e shows the Nyquist plots for the GNP/ZnO-NT and pristine ZnO-NT photoanodes. The near-linear part at low frequency represents the diffusion-limited process, while the diameter of the semicircle at higher frequency is generally related to the underlying electron-transfer limited process. Using an equivalent circuit that includes the electrolyte resistance between the working and reference electrodes (R_s), Warburg impedance (Z_W), double-layer capacitance (C_{dl}) and the charge-transfer resistance (R_{ct}) to model the observed curves, the R_{ct} values for the GNP/ZnO-NT and pristine ZnO-NT photoanodes are determined.[36] The smaller charge-transfer resistance for the GNP/ZnO-NT photoanode (1.60 kΩ) than that for the pristine ZnO-NT photoanode (1.98 kΩ) indicates a more efficient charge-transfer process for the GNP/ZnO-NT photoanode than the pristine ZnO-NT photoanode. The enhanced charge-transfer process confirms that the formation of a Schottky diode at the Au/ZnO interface has a significant effect on the photovoltaic performance.

3.2. Comparison of photovoltaic performance of GNP/ZnO-NT *vs.* pristine ZnO-NT photoanodes

Using the GNP/ZnO-NT photoanode and pristine ZnO-NT photoanode, four different cell structures are constructed with

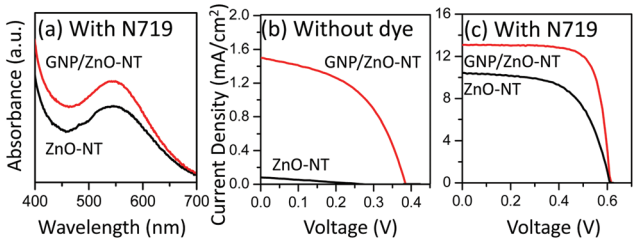

Fig. 5 (a) UV-Vis absorption spectra of GNP/ZnO-NT and pristine ZnO-NT photoanodes with the N719 dye, and the current density *vs.* the voltage curves for solar cells constructed from GNP/ZnO-NT and pristine ZnO-NT photoanodes (b) without and (c) with the N719 dye.

and without the dye loading step. To investigate the cell performance, the photon absorption efficiencies of the two photoanodes are examined. Fig. 5a compares their UV-Vis absorption spectra, which show 25% higher photon absorption for the GNP/ZnO-NT relative to the pristine ZnO photoanode. In Fig. 5b, the current density *vs.* the voltage performance of the solar cells constructed with the GNP/ZnO-NT and pristine ZnO-NT photoanodes in the absence of the N719 dye are compared. Evidently, the short-circuit current density, open-circuit voltage, fill factor and photon conversion efficiency of the pristine ZnO-NT cell have increased, respectively, from 0.07 mA cm^{-2} to 1.5 mA cm^{-2}, from 0.187 V to 0.385 V, from 0.27 to 0.49, and from 0.004% to 0.028% for the GNP/ZnO-NT cell. The higher photon absorption as a result of the plasmonic effect introduced by the GNPs is therefore responsible for the discernible enhancement in the solar cell performance (even without the dye). Fig. 5c shows that upon loading with the N719 dye, the short-circuit current density has increased from 10.4 mA cm^{-2} for the pristine ZnO-NT cell to 13.1 mA cm^{-2} for the GNP/ZnO-NT cell. The corresponding photon conversion efficiency has also increased from 4.7% for the former to 6.0% for the latter. This is a direct result of the higher photon absorption provided by the GNPs.

The size dependence of the plasmon absorption of gold nanoparticles has been studied in the earlier work, which showed that plasmonic Au NPs with an average particle size greater than 16 nm could provide a bigger enhancement at a longer wavelength, while smaller NPs of 10 nm in size would have better absorption at a shorter wavelength, especially in the visible regime.[37] Another study has also shown that smaller plasmonic silver nanoparticles, with an average diameter less than 25 nm in the intrinsic size regime, would exhibit an increased plasmon bandwidth.[38] In accord with these reports, our present results show that the best performance is observed for smaller GNPs (less than 25 nm) while GNPs larger than 30 nm have led to poorer cell performance. This is likely caused by the agglomeration of the larger GNPs, which reduces the total illumination area of the exposed surfaces of the NPs, and by filling of the ZnO tubular structures, which results in poor dye loading. In addition, smaller GNPs would produce a greater shift in the Fermi level due to the small electron accumulation in the GNPs. This is in contrast to the larger, agglomerated GNPs, which would require a larger electron build-up to cause an upward shift of the Fermi level and therefore a higher recombination loss of the accumulated electrons with the oxidized redox electrolyte and/or dye species (the mechanism of which will be discussed below). Consequently, this would produce a lower photocurrent[39,40] and poorer overall performance as shown in Fig. S2, ESI.†

The photon-to-electron conversion mechanisms using the GNP/ZnO photoanode without a dye and that loaded with the N719 dye are shown schematically in Fig. 6. The presence of GNPs would enhance photon absorption in the visible region. As for the case of the GNP/ZnO photoanode without the dye shown in Fig. 6a, electrons are injected from the Au Fermi level to the conduction band (CB) of ZnO upon light illumination, which is responsible for the photocurrent so produced. On the other hand, when the GNP/ZnO photoanode loaded with the N719 dye (Fig. 6b), electron injection into the ZnO conduction band could occur in two routes. The electrons generated from the photo-excited dye molecules, *via* the highest occupied molecular orbital (HOMO) to the lowest unoccupied molecular orbital (LUMO) transitions, could be transported directly to the ZnO conduction band. Alternatively, the generated electron could also be transferred indirectly to the deposited Au NPs first and then onto the ZnO NT surface. As a result of their electron accumulation at the Au energy level, the Au Fermi level would be shifted upward toward the ZnO conduction band, hence resulting in the buildup of a potential barrier at the metal/semiconductor interface. In addition, the existence of the Schottky barrier would enhance the device performance due to the blockage of the back electron-transfer from the ZnO conduction band to the GNPs,[37] which would reduce the recombination loss that may occur between the charge carriers (electrons) and any oxidized species of the redox electrolyte or the dye molecules. The GNP/ZnO-NT

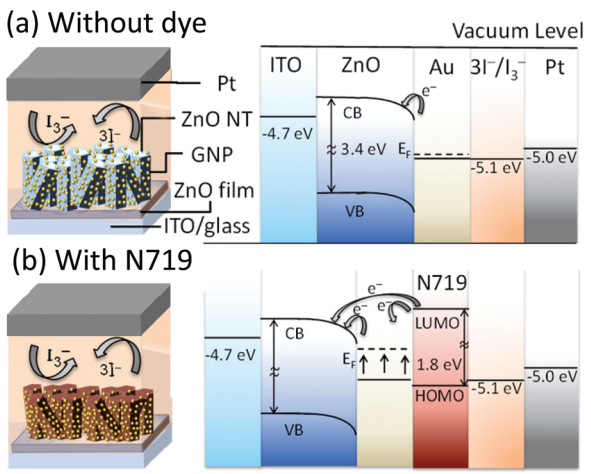

Fig. 6 Schematic diagrams of the device architectures and corresponding energy band diagrams for solar cells constructed from the GNP/ZnO-NT photoanode (a) without and (b) with the N719 dye, illustrating the respective photon-to-electron conversion mechanisms.

system so constructed therefore provides a more efficient charge-transfer process with enhanced light absorption, thus leading to a better overall performance of GNP surface-modified photoanodes.[5]

Future studies could be performed to optimize the vertical arrangement with a fixed spacing of the nanostructures using nanotemplating and nanolithography techniques, in order to increase the charge collection properties and to further enhance the overall performance. An additional step of coating the gold nanoparticles with a passivation layer of an appropriately optimized thickness to prevent them from acting as charge recombination centers could also improve their overall efficiency.

4 Conclusions

By taking advantage of the plasmonic effect, appropriately sized GNPs electrodeposited on ZnO-NTs have provided significant enhancement to their performance in DSSC application. Here, we illustrate that two main enhancements could be achieved by an all-electrodeposition approach. First, a simple, direct electrodeposition technique has been used to deposit ZnO nanotubes, which provide a distinctly higher total surface area (with both inside and outside tubular surfaces) for superior dye loading. Second, electrodeposition is also used to control the deposition of GNPs of an appropriate size that would manifest the plasmonic effect to maximize the optical improvement observed in the visible region. The formation of the interfacial Au/ZnO Schottky barrier also blocks the back electron-transfer from the ZnO conduction band to the GNPs, thereby reducing the recombination loss involving oxidized dyes and/or electrolyte molecules. These enhancements have led to an excellent photon conversion efficiency of 6%, with an open-circuit voltage of 0.61 V and a fill factor of 0.75.

Acknowledgements

This work was supported by the Natural Sciences and Engineering Research Council of Canada.

Notes and references

1 S. Berweger, J. M. Atkin, X. G. Xu, R. L. Olmon and M. B. Raschke, *Nano Lett.*, 2011, **11**, 4309–4313.
2 C. Langhammer, *SPIE Newsroom*, 2012.
3 E. C. Dreaden, A. M. Alkilany, X. Huang, C. J. Murphy and M. A. El-Sayed, *Chem. Soc. Rev.*, 2012, **4**, 2740–2779.
4 G. L. Liu, *IEEE J. Sel. Top. Quantum Electron.*, 2010, **16**, 662–671.
5 A. Bhattacharya, V. P. Rao, C. Jain, A. Ghose and S. Banerjee, *Mater. Lett.*, 2014, **117**, 128–130.
6 P. Georgiev, A. Bojinova, B. Kostova, D. Momekova, T. Bjornholm and K. Balashev, *Colloids Surf., A*, 2013, **434**, 154–163.
7 R. Elghanian, J. J. Storhoff, R. C. Mucic, R. L. Letsinger and C. A. Mirkin, *Science*, 1997, **277**, 1078–1081.
8 D. Li, J. T. McCann, M. Gratt and Y. Xia, *Chem. Phys. Lett.*, 2004, **394**, 387–391.
9 C. S. Chou, R. Y. Yang, C. K. Yeh and Y. Lin, *J. Powder Technol.*, 2009, **194**, 95–105.
10 H. A. Atwater and A. Polman, *Nat. Mater.*, 2010, **9**, 205–213.
11 R. A. Pala, J. White, E. Barnard, J. Liu and M. L. Brongersma, *Adv. Mater.*, 2009, **21**, 3504–3509.
12 Y. A. Akimov, K. Ostrikov and E. P. Li, *Plasmonics*, 2009, **4**, 107–113.
13 P. Spinelli, V. E. Ferry, J. Van de Groep, M. Van Lare, M. A. Verschuuren, R. E. I. Schropp, H. A. Atwater and A. Polman, *J. Opt. Technol.*, 2012, **14**, 024002–024011.
14 V. E. Ferry, M. A. Verschuuren, H. B. T. Li, E. Verhagen, R. J. Walters, R. E. I. Schropp, H. A. Atwater and A. Polman, *Opt. Express*, 2010, **18**, A237–A245.
15 V. E. Ferry, J. N. Munday and H. A. Atwater, *Adv. Mater.*, 2010, **22**, 4794–4808.
16 S. Pillai and M. A. Green, *Sol. Energy Mater. Sol. Cells*, 2010, **94**, 1481–1486.
17 E. Stratakis and E. Kymakis, *Mater. Today*, 2013, **16**, 133–146.
18 J. Zhu, M. Xue, H. Shen, Z. Wu, S. Kim, J. J. Ho, A. Hassani-Afshar, B. Zeng and K. L. Wang, *Appl. Phys. Lett.*, 2011, **98**, 151110.
19 F. C. Chen, J. L. Wu, C. L. Lee, Y. Hong, C. H. Kuo and M. H. Huang, *Appl. Phys. Lett.*, 2009, **95**, 013305.
20 V. Kochergin, L. Neely, C. Y. Jao and H. D. Robinson, *Appl. Phys. Lett.*, 2011, **98**, 133305.
21 Q. Gan, F. J. Bartoli and Z. H. Kafafi, *Adv. Mater.*, 2013, **25**, 2385–2396.
22 B. O'Regan and M. Grätzel, *Nature*, 1991, **353**, 737–740.
23 M. D. Brown, T. Suteewong, R. S. S. Kumar, V. D'Innocenzo, A. Petrozza, M. M. Lee, U. Wiesner and H. J. Snaith, *Nano Lett.*, 2011, **11**, 438–445.
24 J. A. Anta, E. Guillén and R. Tena-Zaera, *J. Phys. Chem. C*, 2012, **116**, 11413–11425.
25 M. McCune, W. Zhang and Y. Deng, *Nano Lett.*, 2012, **12**, 3656–3662.
26 S. H. Ko, D. Lee, H. W. Kang, K. H. Nam, J. Y. Yeo, S. J. Hong, C. P. Grigoropoulos and H. J. Sung, *Nano Lett.*, 2011, **11**, 666–671.
27 M. Abd-Ellah, N. Moghimi, L. Zhang, N. F. Heinig, L. Zhao, J. P. Thomas and K. T. Leung, *J. Phys. Chem. C*, 2013, **117**, 6794–6799.
28 C. H. Ku and J. J. Wu, *Appl. Phys. Lett.*, 2007, **91**, 093117.
29 R. Bhattacharjee and I. M. Hung, *ECS Solid State Lett.*, 2013, **2**, Q101–Q104.
30 C. K. N. Peh, L. Ke and G. W. Ho, *Mater. Lett.*, 2010, **64**, 1372–1375.
31 S. D. Standridge, G. C. Schatz and J. T. Hupp, *Langmuir*, 2009, **25**, 2596–2600.
32 Z. Chen, Y. Tang and C. Liu, *J. Phys. Chem. C*, 2009, **113**, 13433–13437.
33 H. Kidowaki, T. Oku and T. Akiyama, *J. Phys.: Conf. Ser.*, 2012, **352**, 012022–012025.

34 K. Kotsis and V. Staemmler, *Phys. Chem. Chem. Phys.*, 2006, **8**, 1490–1498.
35 J. F. Moulder, W. F. Stickle and P. E. Sobol, *Handbook of X-Ray Photoelectron Spectroscopy*, ed. J. Chastain, Physical Electronics Inc., Eden Prairie, 2nd edn, 1992.
36 J. R. Macdonald, *Impedance Spectroscopy: Theory, Experiment, and Applications*, ed. E. Barsoukov, Wiley, Hoboken, 2nd edn, 2007.
37 S. Link and M. A. El-Sayed, *J. Phys. Chem. B*, 1999, **103**, 4212–4217.
38 S. Pillai, K. R. Catchpole, T. Trupke and M. A. Green, *J. Appl. Phys.*, 2007, **101**, 1–9.
39 X. Hu and D. J. Blackwood, *J. Electroceramics*, 2006, **16**, 593–598.
40 T. Bora, H. H. Kyaw, S. Sarkar, S. K. Pal and J. Dutta, *Beilstein J. Nanotechnol.*, 2011, **2**, 681–690.